



# Mapping deformations and inferring movements of masonry arch bridges using point cloud data

C. Ye<sup>a</sup>, S. Acikgoz<sup>b</sup>, S. Pendrigh<sup>a</sup>, E. Riley<sup>a</sup>, M.J. DeJong<sup>a,\*</sup>

<sup>a</sup> Department of Engineering, University of Cambridge, Cambridge CB2 1PZ, United Kingdom

<sup>b</sup> Department of Engineering Science, University of Oxford, 17 Parks Road, Oxford OX1 3PJ, United Kingdom

## ARTICLE INFO

### Keywords:

Masonry arch bridge  
Support movement  
Point clouds  
Primitive fitting

## ABSTRACT

Many historic masonry arch bridges experience damage due to support movements during their lifetime. This damage may influence the performance of the bridge and reduce its load carrying capacity. This paper proposes a new method to quantify past support movements by investigating distortions in bridge geometry. In this method, the bridge geometry is recorded in point cloud format and segmented into different structural components (e.g. 3D piers and barrels or 2D pier and barrel cross-sections). The geometry of each component is investigated further by fitting primitive shapes (e.g. 3D planes and cylinders or 2D lines and arcs) which represent the design intent. The discrepancy between these fitted shapes and the point clouds reveals a characteristic distortion signature. This signature is compared with theoretical distortion traces, which are obtained from kinematical analyses of the arch subjected to a range of support movements. The most likely support movement scenarios identified from these comparisons are then validated with visual indications of damage, such as crack location and size, and other geometric quantities, such as the change of the bedding joint elevations along the bridge. The proposed technique is applied to two masonry rail viaducts in the UK, which demonstrate different evidence of damage. Using the proposed method, past support movements of both bridges, which led to the observed damage, are inferred.

## 1. Introduction

Masonry arch bridges are an integral part of Europe's rail, road and waterway infrastructure. According to a recent study, 60% of the European rail bridge stock is constructed of masonry. In the UK, the rail network includes approximately 18,000 masonry bridges [1]. These structures have endured increasing load demands throughout the 20th century. While this loading may not exceed the ultimate capacity, most masonry bridges experience damage or deterioration for service loading well below their predicted ultimate capacity. Service level damage may be initiated by, or exacerbated by, deformations caused by support movements or material degradation caused by environmental loading. Thus, the combination of increased loading, support movements, and material degradation can cause increased deterioration rates. This eventually causes their safety to be questioned as further damage continues to decrease their ultimate load carrying capacity. This is clearly demonstrated in a survey performed by Zoltan [1], where representatives of several European railways report the frequent occurrence of relative movement of structural components (e.g. spandrel walls and foundations) while damage due to overloading is rarely

observed.

Assessment of the load carrying capacity of damaged masonry bridges is a challenging task [2]. Before carrying out an assessment of the capacity of a bridge, it is necessary to identify its loading history and model the existing damage [3]. Due to the large uncertainties involved in modelling the formation of damage, conservative methods have been developed to account for commonly observed damage types in structural assessments. For instance, the influence of spandrel walls on the load carrying capacity of masonry arches are typically neglected, since spandrel wall detachment is commonly observed [3]. In a similar way, longitudinal cracks in masonry arches are assumed to limit the effective bridge width [4].

However, many other types of damage in masonry bridges cannot be accounted for using simple assumptions. In particular, many historic masonry arch bridges experience damage due to support movements during their lifetime [3,5]. Support movements involving relative horizontal and vertical displacements or rotations of bridge piers may occur during construction, notably during the removal of bridge centring [5,6]. Similarly, progressive support movements may occur during the service life of the bridge, for example due to soil consolidation,

\* Corresponding author at: Department of Engineering, University of Cambridge, Trumpington Street, Cambridge CB2 1PZ, United Kingdom.

E-mail address: [mjd97@eng.cam.ac.uk](mailto:mjd97@eng.cam.ac.uk) (M.J. DeJong).

<https://doi.org/10.1016/j.engstruct.2018.06.094>

Received 7 December 2017; Received in revised form 18 April 2018; Accepted 25 June 2018

Available online 11 July 2018

0141-0296/ © 2018 The Authors. Published by Elsevier Ltd. This is an open access article under the CC BY license (<http://creativecommons.org/licenses/by/4.0/>).

environmental effects and cyclic loading of foundations. These movements may not be visible to the naked eye, and may have different influences on the response mechanisms of the bridge [7], and the resulting observable damage. Therefore, quantifying support movements is a necessary step for improving the capacity assessment of damaged masonry bridges.

This paper proposes a new assessment method to map 3D deformations and identify the historic support movements of a bridge by evaluating existing bridge distortions. In this method, the distorted bridge geometry is quantified using laser scanning technology and point cloud processing. The method involves processing of the point cloud by: (i) segmenting it into bridge components, (ii) fitting suitable primitives to each component, and (iii) describing the discrepancy of the actual and fitted geometries with 2D and 3D error maps. In order to determine historic support movements using the error maps, a theoretical arch mechanism database is created. This database quantifies distortions of kinematic arch models using a wide range of support movements. It is proposed that comparisons between the error maps, theoretical mechanisms and visual signs of damage may help identify the most likely support movements experienced by the bridge. Finally, the proposed technique is applied to two damaged masonry rail viaducts in the UK: Marsh Lane Viaduct in Leeds and Stapleton Road Viaduct in Bristol.

## 2. Applications of laser scanning for structural assessments

Laser scanning describes a method of non-contact sampling of the shape and appearance of an object using laser technology. Lasers are ideally suited for this purpose, since they do not require ambient lighting or surface features for sampling. A number of different scanning techniques can be used to scan real-world objects [8]. Modern scanners have acquisition times of hundreds of thousands of points per second and this allows capturing a 3D environment with a dense point cloud in a matter of minutes, although post-scanning registration can require significant post-processing times.

In the last two decades, laser scanning has found widespread application in the documentation of heritage masonry structures (e.g. [9]). Since detailed construction drawings are rarely available for masonry arch bridges, laser scanning has been widely used to quantify the external geometry of the structure. Achieving this requires denoising the data and identifying different bridge components (e.g. arch barrel) using manual and automated processing techniques [10]. Key geometry components such as span and rise are then determined from distance measurements on relevant parts of the clouds (e.g. [11,12]). While manual measurements can be used to retrieve distance measurements between identified objects on a point cloud, automated algorithms which measure closest [13] or normal [14] distance between sets of points, meshes and analytical surfaces can also be utilised. This critical geometry information can later be used in the quantitative assessment of the bridge [12].

Another relevant application of laser scanning for masonry arch bridge assessment concerns direct assessment of geometry data for structural purposes. Previous studies in this area can be divided into two broad categories. First category involves detailed analysis of the distorted structural geometry from a point cloud via primitive shape fitting. The characteristics of the fitted shape, and its comparison to the actual point cloud, can be useful to infer important phenomena concerning structural behaviour of the asset. The studies in the second category focus on calculating precise displacements by comparing point clouds [14,15]. This approach is especially useful to monitor structural response of masonry bridges during nearby construction works by comparing point clouds before and after construction [7,16]. Since this paper is concerned with determining historic settlements, where limited data concerning the original design of the bridge is available, the following literature review focuses on the first category.

When boundary conditions of the structure and loading types are known, theoretical analyses of simple structures (e.g. beams, portal

frames) can provide a generic description of deflected shapes that the structure may be expected to experience. These generic shapes (e.g. polynomials) can then be fitted to the point cloud data to identify the deformation experienced and to infer the loading [17,18]. However, it is difficult to ascertain boundary conditions for masonry arch bridges, and reliably relate their internal deflections to given support movements. In such cases, a fitted geometry can be evaluated to highlight ‘anomalies’ in the observed point clouds. In three recent works [19–21], tower facades and cross-sections were characterised with planar and circular shapes, in order to highlight change of cross-section properties along height as well as the leaning angle of the tower. Comparisons between fitted geometry and the actual point cloud complemented this information by highlighting local anomalies in the cloud, such as bulging, brick displacement or material loss. Shape-fitting was also used to evaluate distortions of historic masonry structures, including domes and vaults [22].

Due to the lack of construction drawings, it is more challenging to identify anomalies observed in point clouds of masonry arch bridges. For instance, it is well-known that asymmetric bridges with different springing heights were commonly constructed to deal with uneven terrain conditions. In their study, Armesto et al. [23] have proposed an algorithm for the non-parametric estimation of arch shape and determined significant asymmetry in the bridge. However, it is not certain if this asymmetry relates to a structural phenomenon or the original design of the bridge. More recently, Conde et al. [24] have solved this issue by determining the original shape of the masonry arch and the unknown settlements by an optimisation process aimed to capture the deflected shape of the structure obtained from the laser scan. Despite these recent advances, there still remains a need for simple cloud processing methods which can identify distortions and relate them to support movements of the structure. A method to achieve this objective is proposed in the next section.

## 3. A new assessment method to estimate historic support movements of masonry arch bridge

In this section, a new method is proposed to estimate historic support movements of masonry arch bridges. The workflow associated with this new method is schematically described in Fig. 1 and discussed systematically in the following sections. Capturing the bridge geometry with a laser scan requires an initial understanding of the bridge characteristics. Therefore, the first step of this method involves collecting preliminary information on the bridge.

### 3.1. Preliminary bridge information – Step 1

Preliminary bridge information may be retrieved from construction drawings, inspection reports and field measurements. This includes the form of the bridge (e.g. square or skew), the basic arch shape (e.g. segmental or elliptical), fundamental arch and pier geometry (e.g. span, rise and springing height). Field work can complement this information by highlighting the bridge defects such as cracks and the remedial works such as repointing.

### 3.2. Laser scanning data acquisition and point cloud processing – Step 2

Preliminary bridge information provided in Step 1 can be used to plan the laser scanning data acquisition. Once the laser scan data has been gathered, the raw point cloud data needs to be processed for primitive shape fitting (Step 3). The processing consists of five stages: registration, cleaning, sampling, segmentation and alignment. During the registration step, multiple laser scans are combined together to obtain one single point cloud which contains the entire bridge. This was achieved using FARO SCENE for this study (Version 6.0, Lake Mary, FL, USA). In Fig. 2a, an example point cloud of a masonry railway viaduct is shown.

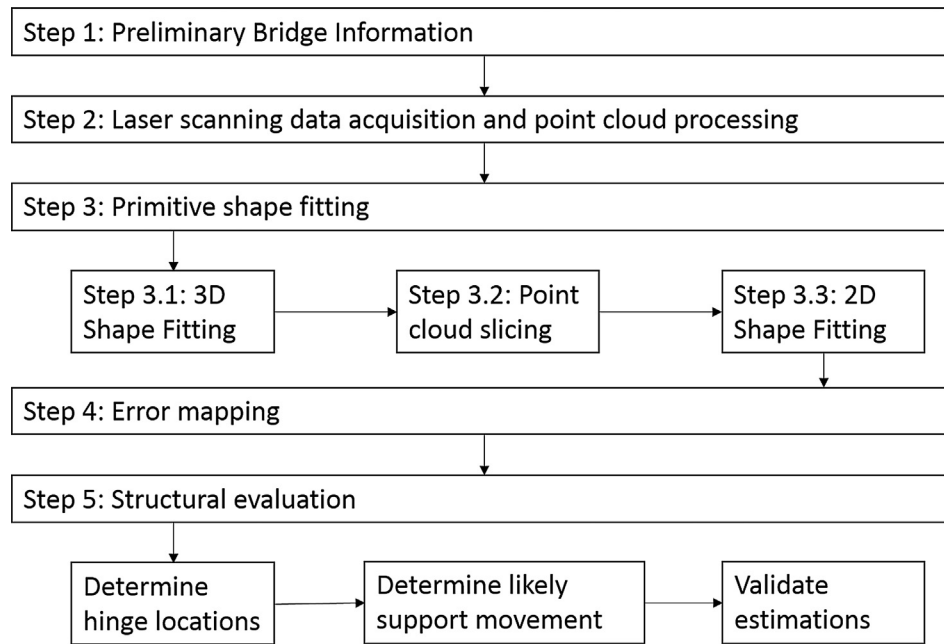


Fig. 1. General workflow of the developed assessment method.

Next, point cloud cleaning is performed to manually crop out unwanted features (e.g. plants, parapet walls, neighbouring buildings). Then, the point cloud data is sampled in order to (i) remove outlier points and (ii) achieve a uniform data spacing between neighbouring points, which allows for quick and accurate post-processing. These can be achieved by using the established filtering, subsampling and re-sampling tools in point cloud libraries, such as Cloud Compare (Version 2.6.2, Clamart, France). Once the clouds are sampled, they are segmented into arch barrel, pier and spandrel wall elements, a process which can be automated [10]. For convenience, the whole cloud is then oriented in the XY plane such that its transverse axis direction, given by the direction vector  $\underline{u} = (u_x, u_y, u_z)$ , is aligned with the vector  $(1, 0, u_z)$  where  $u_z$  is a measure of the transverse inclination of the arch. An arbitrary point  $(x_0, y_0, z_0)$  might also be defined, which is located on the arch transverse axis. The processed point cloud is illustrated in Fig. 2b.

### 3.3. Primitive shape fitting – Step 3

The processed and segmented point clouds can be used for primitive shape fitting. A systematic approach is described below where 3D fits are conducted in Mathworks Matlab software (Version 8.0, Natick, MA,

USA). Using the results of the 3D fit, the point clouds are sliced in 2D cross-sections along the bridge longitudinal and transverse axes. These slices are then fitted with 2D shapes.

#### 3.3.1. 3D shape fitting – Step 3A

Since the majority of masonry arch bridges are segmental constructions with originally straight-faced piers, the developed algorithms are designed to fit planes and cylinders in 3D. Algorithms have also been extended to account for other shapes, such as ellipse fitting to evaluate geometry of masonry vaults [22] and distortion of elliptical arches [25] or skew arches, but are not discussed here. In the following, the utilised shapes and their associated fitting algorithms are presented.

**Plane fit:** Plane fit is used for evaluating pier and spandrel wall surfaces and is primarily used to determine pier plane surface normals  $(n_x, n_y, n_z)$ . For idealised square span bridges, the vector  $(n_x, n_y, 0)$  may be expected to align with the longitudinal axis of the bridge (see Fig. 2b). The plane fit algorithm minimises the normal distance between the fitted plane and individual points by performing Singular Value Decomposition on the point cloud matrix [26]. The unit  $(n_x, n_y, n_z)$  vector can then be determined from  $(A, B, C)$  (see Table 1).

**Cylinder fit:** A cylinder is used to fit the arch intrados in order to

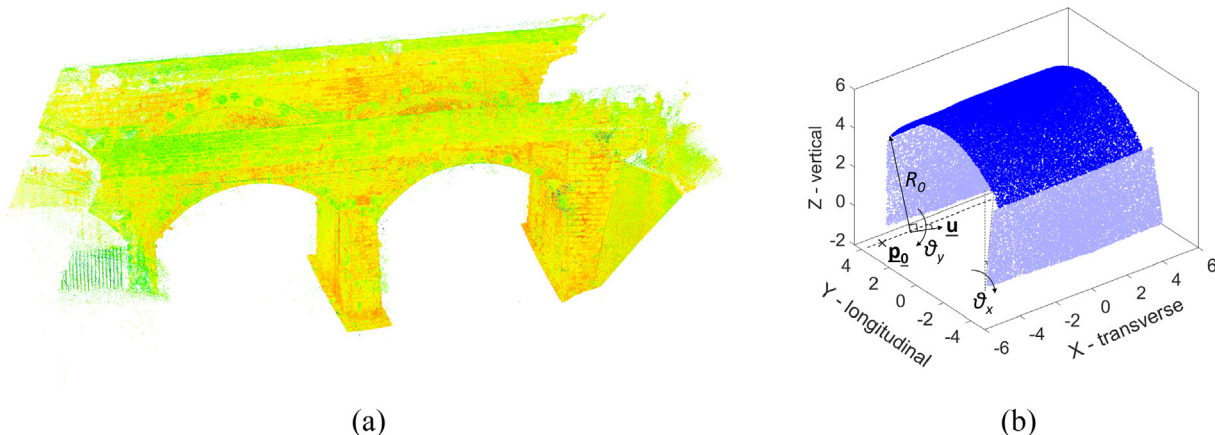
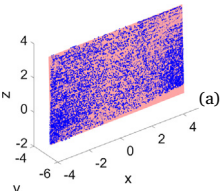
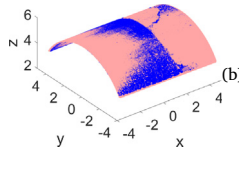
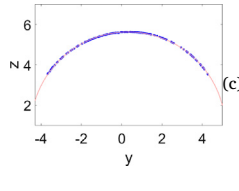


Fig. 2. (a) An example of a registered and raw point cloud of a masonry viaduct consisting of segmental arches with a square span (point colour depicts backscatter laser intensity) and (b) one span of the viaduct after point cloud processing.

**Table 1**  
Shape fitting.

	Plane fit	3D circular cylinder fit	2D circle fit
Diagram			
Equation (vector form)	$(\mathbf{p} - \mathbf{p}_0) \cdot \mathbf{n} = 0$ where $\mathbf{n} = (n_x, n_y, n_z)$ is the normal vector of the plane, $\mathbf{p}_0 = (x_0, y_0, z_0)$ is a point on the plane, and $\mathbf{p} = (x, y, z)$ is a point of the point cloud	$ (\mathbf{p} - \mathbf{p}_0) \times \mathbf{u}  = R_0$ where $R_0$ is the radius, $\mathbf{u} = (u_x, u_y, u_z)$ is the unit direction vector of the arch transverse axis $\mathbf{p}_0 = (x_0, y_0, z_0)$ is a point on the arch transverse axis and $\mathbf{p} = (x, y, z)$ is a point of the point cloud	$ \mathbf{p} - \mathbf{c}_0  = R_0$ where $R_0$ is the radius, $\mathbf{c}_0 = (y_0, z_0)$ is the centre of the circle, and $\mathbf{p} = (y, z)$ is a point of the 2D point cloud
Equation (Cartesian form)	$Ax + By + Cz + D = 0$	$(y - y_0)^2 + (z - z_0)^2 = R_0^2$ $y^2 + z^2 + Ay + Bz + C = 0$	$(y - y_0)^2 + (z - z_0)^2 = R_0^2$ $y^2 + z^2 + Ay + Bz + C = 0$
Definition of error, $e$ (vector form)	$e = (\mathbf{p}_i - \mathbf{p}_0) \cdot \mathbf{n}$ where $\mathbf{p}_i = (x_i, y_i, z_i)$ is a point of the point cloud	$e = d_i - R_0$ where $d_i =  (\mathbf{p}_i - \mathbf{p}_0) \times \mathbf{u} $ , $\mathbf{p}_i = (x_i, y_i, z_i)$ is a point of the point cloud	$e = d_i - R_0$ where $d_i =  \mathbf{p}_i - \mathbf{c}_0 $ , $\mathbf{p}_i = (y_i, z_i)$ is a point of the 2D point cloud slice
Definition of error, $e$ (Cartesian form)	$e = \frac{Ax_i + By_i + Cz_i + D}{\sqrt{A^2 + B^2 + C^2}}$	$e = \sqrt{\left(y_i + \frac{A}{2}\right)^2 + \left(z_i + \frac{B}{2}\right)^2} - \sqrt{\frac{A^2}{4} + \frac{B^2}{4} - C}$	$e = \sqrt{\left(y_i + \frac{A}{2}\right)^2 + \left(z_i + \frac{B}{2}\right)^2} - \sqrt{\frac{A^2}{4} + \frac{B^2}{4} - C}$

estimate the cylinder radius  $R_0$ , as well as the arch transverse axis vector  $(u_x, u_y, u_z)$ . The developed cylinder fit algorithm minimises the absolute distance between the fitted shape and the points using an unconstrained nonlinear optimisation algorithm, which requires an initial estimation of the cylinder radius, arch transverse axis and an arbitrary point on this axis. Furthermore, the initial alignment of the arch transverse axis vector to  $(1, 0, u_z)$  (see Section 3.2) suggests that an initial guess of  $(1, 0, 0)$  may be used. The estimate for the arbitrary point on the arch transverse axis  $(x_0, y_0, z_0)$  may be determined by using an arbitrary point on the crown of the arch barrel and the initial estimate of radius. It was determined that these estimates provide sufficiently accurate starting points for the nonlinear optimisation.

### 3.3.2. Point cloud slicing for 2D section generation – Step 3B

In order to examine bridge geometry in longitudinal and transverse bridge directions, investigating the geometry of 2D sections of point clouds along these directions are useful. This is achieved by generating lines along the bridge longitudinal and transverse directions and finding the vertical planes that feature these lines. Then all points lying within a distance from this plane are retrieved. The specified distance determines the thickness of the obtained strip. Table 2 demonstrates the point cloud from Fig. 2b after it has been sliced. Pier strips are useful for determining key dimensions such as span and pier thickness along the width of the arch.

### 3.3.3. 2D shape fitting – Step 3C

3D fitting typically reveals if notable geometry changes occur along the transverse length of the bridge (e.g. due to bridge widening or gross differential support movements). In these cases, it can be informative to

explore data from different longitudinal and transverse strips of the bridge along its transverse length (see Table 2). In the case that the bridge transverse slices do not reveal noteworthy differences along the bridge transverse length, a single 2D section can be investigated for detailed analysis.

**2D circle fit:** Data from longitudinal sections of the bridge along its transverse length (see Table 1) can be fitted with circles for segmental bridges. Circle fitting using Kasa's method [27] allows efficient determination of the radius of curvature  $R_0$  of two dimensional datasets without the need for initial parameter estimations. The diagram on subplot c of Table 1 illustrates a circle fitted to a 2D cloud in the YZ plane using the outlined procedure.

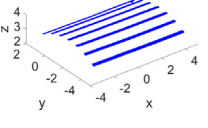
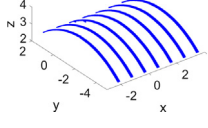
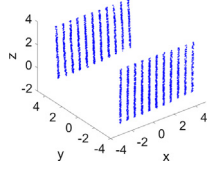
### 3.4. Error mapping – Step 4

Anomalies in bridge geometry can be identified from the properties of fitted shapes discussed in Section 3.3. For instance, inclination in piers may be determined from plane normal vector  $(n_x, n_y, n_z)$ , which may be indicative of support movements. In addition, the comparison between fitted shapes and the actual point cloud may also reveal useful information on geometry distortions. The discrepancy between these two aspects is referred to as 'fitting error' and its visualisation is called 'error mapping'. Fitting errors are quantified mathematically in this section.

#### 3.4.1. Plane fit

The plane fitting procedure minimises the root mean square of the shortest distances between the points and the fitted shape. In the following, the error  $e$  relates to the signed distance between the plane and

**Table 2**  
Point cloud slicing.

	Transverse arch strip	longitudinal arch strip	Pier strip
'2D' strips			



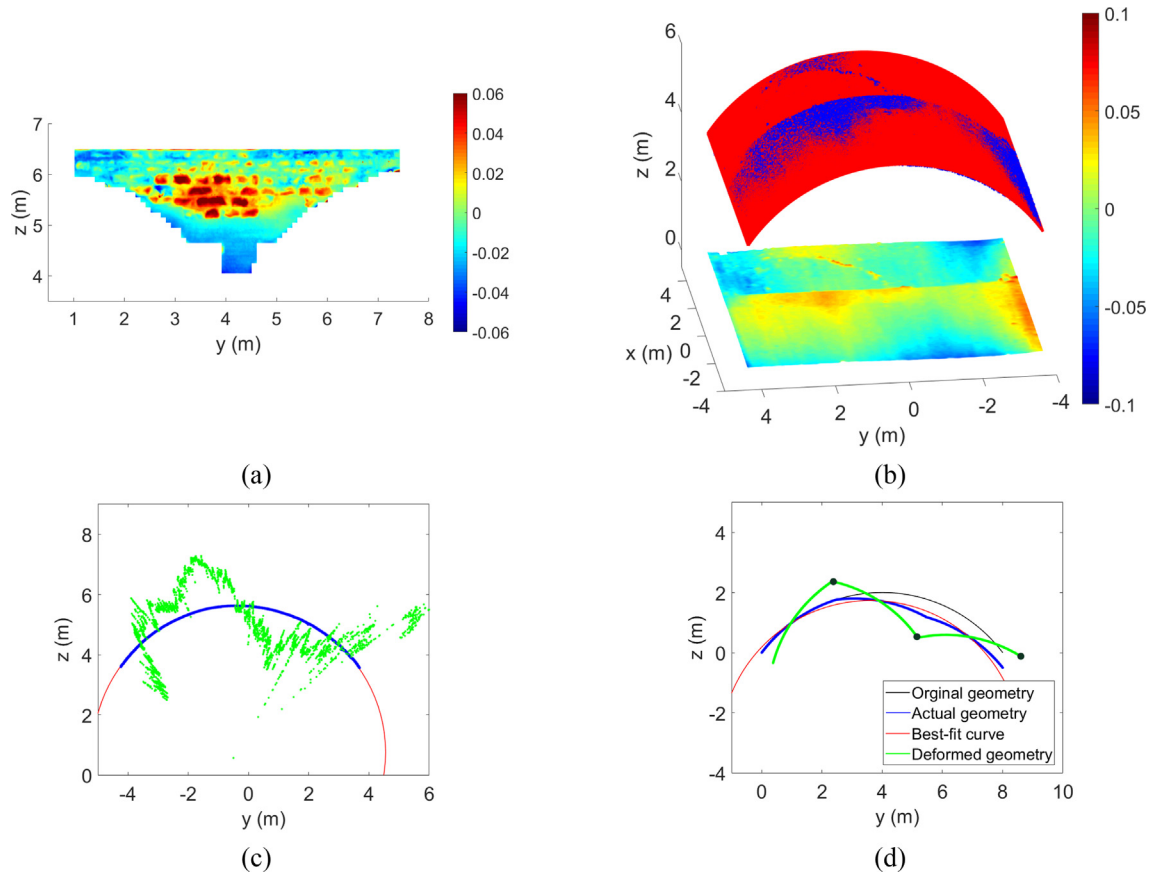


**Fig. 3.** (a) Example 3D error map for plane fit of a spandrel wall, (b) example 3D error map for cylinder fit of an arch, (c) example 2D error map (error magnification factor of 100) and (d) schematic explanation of 2D error map components (error magnification factor of 100, black dots = plastic hinges).

the point along the plane surface normal vector  $\mathbf{n}$ . To do this, vectors referring to the locations of arbitrary points from the cloud  $\mathbf{P}_i$  and the plane  $\mathbf{p}_0$  are defined. The following equation then describes the error in vector format:

$$e = (\mathbf{P}_i - \mathbf{p}_0) \cdot \mathbf{n} \quad (1)$$

where the operator describes dot product. Positive error indicates that the normal distance between the point and the plane is positive. An example plane fit error map is shown in Fig. 3a, in which bulging of the spandrel wall (shown with areas in red) is clearly evident.

#### 3.4.2. 3D cylinder fit

In a similar manner to the plane fit, 3D cylinder fitting procedure minimises the root mean square of the shortest distances between points and the fitted shape. However, since the cylinder surface normal direction changes, the error  $e$ , which represents the normal distance between the point and the fitted shape, can be determined from

$$e = |(\mathbf{P}_i - \mathbf{p}_0) \times \mathbf{u}| - R_0 \quad (2)$$

where  $\mathbf{P}_i$  represents the position vector of a single point in the point cloud,  $\mathbf{p}_0$  represents the position vector of an arbitrary point situated on the transverse axis of the fitted cylinder, and  $\mathbf{u}$  is the unit vector in the direction of the same transverse axis. An example of an error map produced from a 3D cylinder fit is shown in Fig. 3b. In this figure, the fitted shape (red) and the 3D point cloud (blue) are shown and the 2D colour map underneath shows the projection of the errors in the XY plane. To generate the 2D colour map, the “GridFit” function in Matlab (John D’Errico, 2016) was utilised. In this colour map, points that lie above the best-fit surface are depicted with colours towards the red end of the spectrum; while points that lie below are depicted by colours towards the blue end of the spectrum.

#### 3.4.3. 2D circle fit

2D circle fit is a special case of the more general 3D cylinder fit. Therefore, the previous Equation 2 can also be used to calculate error in the radial direction. An example of an error map produced from a 2D cylinder fit is shown in Fig. 3c. In this figure, the fitted shape (red) and the 2D point cloud slice in the YZ plane (blue) are shown. In addition, the green points represent shifted blue points by magnifying the radial error by 100 times. A magnification factor of 100 will be used throughout this paper to visualise the distortions.

#### 3.5. Structural evaluation – Step 5

The primitive shape fitting and the following error mapping do not provide direct information on the historic support movements experienced by the structure for two main reasons. First, the reference as-built geometry, or even the design geometry, are typically not known. To understand how the fitted geometry parameters may relate to the reference as-built geometry, reasonable assumptions informed by typical construction practices need to be made (Section 3.5.1). Second, although the error maps produced may have been caused by support movements or bulging, the errors are actually artefacts of fitting an ideal cylinder to a distorted shape by minimising error. Therefore, the pattern of the error map produced needs to be evaluated further to relate the errors to particular structural behaviour and support movements. This, in return, requires making assumptions concerning bridge deformation behaviour (Section 3.5.2) and modelling distortions with structural models to correlate the observed fitting errors to real support movements (Section 3.5.3).

##### 3.5.1. Reference bridge geometry assumptions

To evaluate the fitted shape parameters, it is necessary to formulate

**Table 3**  
Examples of reference geometry and deformation assumptions used to interpret results.

	Reference geometry	Deformation
Piers	i. Pier surfaces under an arch are planar and parallel. The horizontal component of the surface normal vector aligns with the bridge longitudinal axis. ii. For a vertically straight pier, the out of plane inclination $\theta_x = 0$ for two pier side-wall surfaces. iii. For a tapered pier, $\theta_x = 0$ for the mean plane of the two pier side-wall surfaces.	i. Non-zero rigid body rotation of the pier in $\theta_x$ direction causes span opening and closing. ii. Where original abutments are inclined, it is not possible to estimate potential support movements. In these cases, abutments were assumed to be more stiff than piers, so relative support movements were assumed to be caused by pier support movements.
Arches	i. The arch is a uniform cylinder with a circular longitudinal cross-section and a straight line transverse cross-section. The arch transverse axis aligns with bridge transverse axis. ii. The arch has a square span with negligible skew.	i. Masonry behaviour is assumed as rigid-plastic and the arch responds to support movements as a mechanism. ii. Up to three hinges may appear at arch springing, quarter span, 1/3rd span or crown points to facilitate the kinematic response to support movements. iii. Anomalies in the transverse section cuts indicate differential settlements along the transverse direction
Spandrel walls & Pier ends	i. Spandrel wall surfaces are planar. Their normal aligns with bridge transverse axis. ii. The out of plane inclination $\theta_y = 0$ for the two opposing pier end surfaces.	i. Non-zero rigid body rotation of the spandrel wall and pier end in the $\theta_y$ direction indicates spandrel wall and pier end tilting respectively.

some rough guidelines on the typical construction and design intent for the geometry of different components of masonry arch bridges. This is presented in the second column of Table 3 for most typical masonry bridges, which have a segmental geometry with negligible skew. Note that the shape fitting does not constrain different springing heights on either side of the bridge and allows a linear change of springing height along the bridge transverse direction.

### 3.5.2. Bridge deformation assumptions

Identified irregularities in the geometric characteristics defined in the second column of Table 3 provide strong indications of historic movements. While aspects such as material ageing and water ingress may also influence the local geometry, systematic distortions are typically related to relative movements between structural elements. Therefore, it is reasonable to assume that the distortion patterns are related to support movements, which occur during or just after construction, or later during bridge operation.

Previously, it has been observed that limit analysis methods which treat masonry as rigid-plastic material can sufficiently describe structural response to support movements [7,16]. In these methods, the arch responds to support movements by forming a kinematic mechanism. A similar approach is adopted in this paper where it is assumed that three “hinges” can form in the arch, and these hinges can be located at springing, quarter span, 1/3rd span or crown points. These may appear symmetrically or asymmetrically and account for the distortion observed in the barrel. It must be emphasised that these “hinges” may not occur at discrete points in reality. However, they provide an efficient method to represent a localisation of continuous deformation over a relatively small region with respect to the length scale of the bridge span. Meanwhile, when differential support movements occur along the bridge transverse direction, there may be different mechanisms along the width of the bridge. In these cases, 2D fits are conducted and the elevation of transverse slices are evaluated.

In addition, a similar rigid-plastic approach is used for evaluating movements in piers and spandrel walls. The identified rotations in  $\theta_x$  and  $\theta_y$  indicate relative movement between structural components. Notably, changes in span length can be estimated by multiplying the pier height with the identified fitting parameter for pier rotation  $\theta_x$ . However, care must be exercised when estimating span opening and closing with pier rotations. The pier rotation indicates the relative movement of the pier top with respect to the ground. However, the pier may not have been built vertical. Additionally, in some cases, though unlikely, the pier may be rotating towards the crown of the arch but the span may be opening due to a rigid body translation of the whole pier. In this case, relating the span opening or closing to the magnitude and

direction of pier rotation may be misleading. Therefore, in this paper the magnitude of horizontal springing displacement relative to the ground is estimated using pier rotation data, but this should only be taken as a potential indicator of span opening and closing. For the spandrel wall, a similar approach can be used to quantify spandrel wall tilting with the use of inclination angle  $\theta_y$ . The outlined assumptions concerning the deformation behaviour of the bridge are summarised in the third column of Table 3.

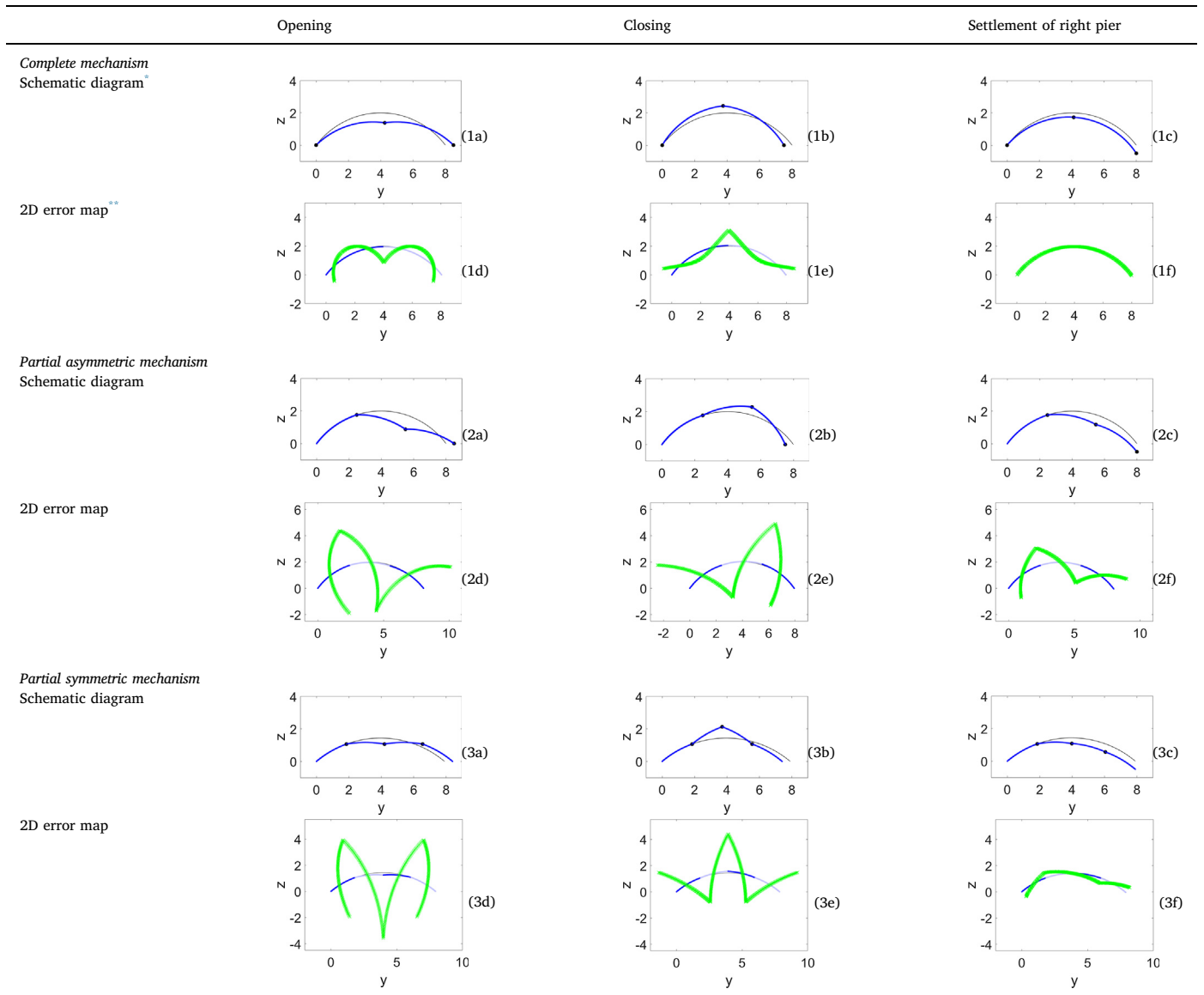
### 3.5.3. Theoretical arch mechanism database

In this section, the assumptions concerning reference bridge geometry and arch deformation (Sections 3.5.1 and 3.5.2) are used to generate 2D kinematic arch models, which are subjected to a range of support movements. By investigating their distorted geometry (after support movements) with 2D circle fits (see Section 3.3.3), error maps similar to those discussed in Fig. 3c are obtained for theoretical models (see Fig. 3d). These investigations reveal characteristic distortions and error map shapes for particular types of support movements. In this section, these shapes are catalogued in a database for future reference, so that the error map resulting from a 2D circle fit of a real masonry bridge can be compared directly with the database in order to identify possible support movement scenarios.

First, the idealised arch geometry that will be examined with theoretical models is specified. The examined radius of curvature and span are similar to the case study arches which will be examined later in Section 4. In particular, each arch has a span of 8 m and a radius of 5 m. Since the following analyses are not sensitive to small differences in initial geometry, it is not critical for these parameters to represent the precise (and unknown) reference geometry. Then, a series of models are created which each include three plastic hinges to accommodate support movements. For simple comparisons with field data, the theoretical arch mechanism assumes that the arch thickness is negligible compared to the arch span. These models cover a realistic range of locations for hinges, which may be located at springing, quarter span, 1/3rd span or crown points, as stated previously. In a complete arch mechanism, such as those presented in subplots 1a–1f of Table 4, the hinges are located at springings and the crown, and all parts of the arch move. In contrast, in a partial arch mechanism, as shown in subplots 2a–2f and 3a–3f, part of the arch between the hinges and springing points does not rotate with respect to the springings. This type of mechanism is generally caused by the presence of backing in arch bridges [6].

After defining the mechanisms, these kinematic models were subjected to different combinations and magnitudes of support movements. For each of these support movement simulations, the rotation of each portion of the arch between the hinges is found by simple trigonometry.

**Table 4**  
Theoretical arch mechanism database.



\* In schematic diagrams: black line = ideal shape, blue line = schematic distorted shape, black dot = plastic hinge.

\*\* In 2D error maps: alternating colours (dark blue and light blue) = distorted shape, green = distorted geometry (magnified 100 times) with respect to the fitted shape.

After the distorted shapes are obtained, they are fitted with a circle. The error maps for these fits are then plotted. An example of this procedure is shown in subplots 1a and 1d of Table 4. Here, the arch span is opening 5 cm, which is accommodated with the well-known three hinge mechanism [5], with hinges at the crown and springing points. The schematic distorted shape (thick blue line) is shown in subplot 1a, with black dots highlighting prescribed hinge locations. Subplot 1d shows the segments between hinges in alternating colours (dark blue and light blue), as well as the errors of the distorted geometry (thick light green, magnified 100 times) with respect to the fitted shape. Note that the distorted shape experiences a sharp kink at the crown location due to the presence of a hinge.

After conducting a range of realistic support movement simulations with different magnitude and different combinations of vertical and horizontal movements, it was determined that the magnitude of support movements does not significantly influence the error map shape. However, the magnitude of distortions increases linearly with the magnitude of support movements. Therefore, in Table 4, all the applied

support displacements are fixed to an arbitrary 5 cm. To capture if the distortions are due to predominantly horizontal and vertical support movements, Table 4 only examines support movements that involve pure horizontal and vertical displacements. Therefore, span opening, closing and relative vertical settlement scenarios are explored. The output of this step reveals support movements which can explain the systematic distortions observed in the bridge.

### 3.5.4. Determining historic deformations

The identified distortions from primitive shape fitting do not relate to support settlements uniquely; it is possible to find different support movements which yield similar distortions. This is observable in subplots 2d–2f of Table 4, where the error map shape identified for the span opening mechanism is nearly identical to the error map shape identified for the settlement of the right pier. These error maps display different magnitudes of distortions, due to the different rotation magnitudes of arch segments between hinges required to accommodate the support movements, despite similar shapes. Therefore, Table 4 demonstrates

that it is not possible to identify the support movements by examining error map shapes alone. Identifying the likely support movements experienced by the bridge requires a more systematic evaluation of all information gathered during the outlined assessment procedure. The following procedure is suggested for this purpose:

- i. Using the error map results of the 2D fit and the generic theoretical arch mechanism database in Table 4, identify the hinge arrangements (e.g. kinks) which may describe the observed bridge distortion.
- ii. From field observations, determine the most likely hinge arrangement by investigating visible signs of hinging on the arch intrados, such as cracking and loose bricks.
- iii. For the chosen hinge arrangement, determine the support movements, which may describe the observed bridge distortion, using the error map results of the 2D fit and the theoretical arch mechanism database in Table 4.
- iv. To identify the most likely support movements, review the assumptions concerning likely bridge deformations in Table 4. In particular, use the following to identify the more likely mechanisms:
  - a. Pier inclination data may indicate span opening and closing.
  - b. Significant drops in arch barrel and spandrel wall bedding joint level may indicate relative vertical settlements.
  - c. Theoretical predictions of hinge locations may be obtained for a given support movement by minimising the work done by support forces during settlement [4]. Evaluate the agreement between the identified hinge locations and support movements from laser scan data with theoretical predictions.
- v. Evaluate 3D error maps to observe if the identified support movements describe the behaviour of the whole arch. If these indicate different behaviour along the transverse direction of the bridge, conduct the previous steps (i)–(iv) for other longitudinal slices to identify support movements along the whole width of the arch.
- vi. Collect evidence of support movements from independent measurements. If the arch is part of a viaduct, examine the geometry of neighbouring arches. Additional dynamic measurements may also provide useful information [28].

To illustrate this approach, two masonry viaducts are examined in the next section. These viaducts display different damage characteristics and provide the opportunity to demonstrate the utility of the proposed approach for different bridges.

## 4. Case studies

### 4.1. Case study 1 – Marsh Lane Viaduct, Leeds

#### 4.1.1. Step 1 – Preliminary bridge information

The Marsh Lane Viaduct is an 1860s masonry arch rail bridge in Leeds, UK (see Fig. 4). Today, it carries two railway tracks. Three spans of the bridge, denoted as Arch 37, 38 and 39, are examined in this paper. Fig. 5b shows a plan view of these spans, which demonstrates a slight curvature of the bridge route. These arches span approximately 7.7 m and are segmental in shape. There is little evidence of skew but the measurements demonstrate that the thickness of piers increase on the northern side to achieve the desired route curvature.

Repairs were completed in September 2015 to strengthen the bridge superstructure. For example, steel ties were installed, bricks were re-pointed for piers and spandrel walls, and the two relieving arches in the two piers were filled with concrete (see Fig. 4b). Prior to this, sagging of the crown of the relieving arch, and the opening of the longitudinal crack above the relieving arch were observed, particularly between Arches 38 and 37. The longitudinal crack branched into two and forms a wedge shaped area where Network Rail have reported loose bricks (Fig. 6a). Site observations additionally revealed the presence of transverse cracks at the western quarter span of Arch 38 and the eastern quarter span of Arch 37 (Fig. 6b). Finally, the spandrel walls of the bridge have experienced significant cracking, particularly in the horizontal direction. Detailed investigation of the dynamic behaviour of the masonry arch with new monitoring techniques highlights the influence of these aspects on the behaviour [28,29].

#### 4.1.2. Step 2 – Laser scan data acquisition and point cloud processing

Laser scan data was collected on July 2015 before the strengthening works with a FARO x330 scanner. The point cloud shown in Fig. 5a was achieved with standard scanning resolution (6 mm point spacing at 10 m distance). The scanner was placed under the centre of each investigated arch, as well as several locations outside it to capture all the bridge components (scanner locations indicated in Fig. 5b with the orange and red dots). To achieve a uniform spatial distribution of points, the data was then resampled. This was followed by the segmentation of the bridge into arch barrel, pier and spandrel wall components.

Another laser scan data acquisition was conducted in October 2016 after the repair works. This time, a Topcon GLS-2000 scanner was used. The computational results from the second set of data were found to be similar to those of the first set. Therefore, in this paper only the results from the first set are presented.

#### 4.1.3. Step 3 – Primitive shape fitting

Planes were fitted to the piers and spandrel walls, while cylinders

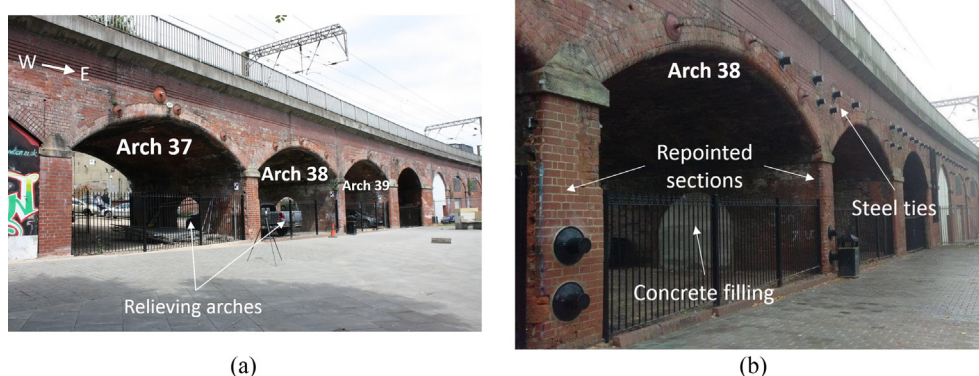


**Fig. 4.** Marsh Lane Viaduct view from the South: (a) view of the investigated arches prior to remedial works and (b) evidence of remedial works: steel ties, masonry repointing and concrete filling of the relieving arches.



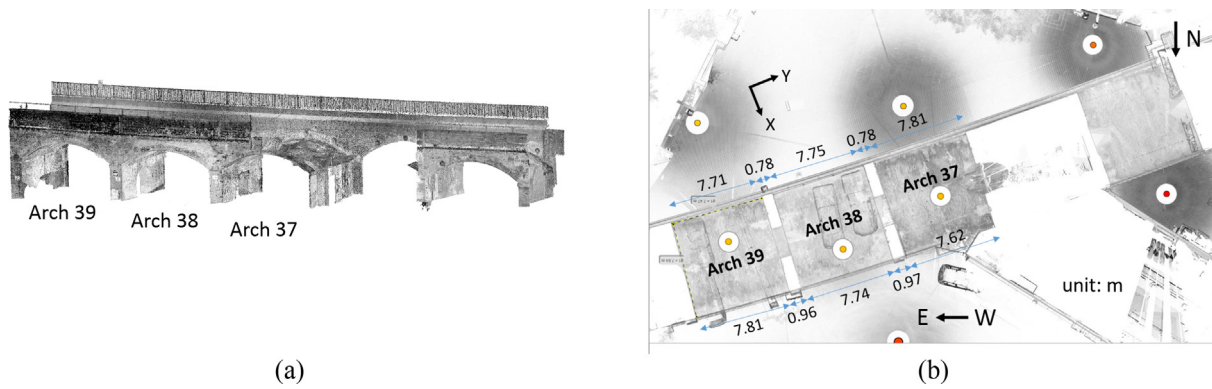


Fig. 5. Marsh Lane Viaduct point cloud: (a) view from the North and (b) view from the top, with key dimensions labelled.

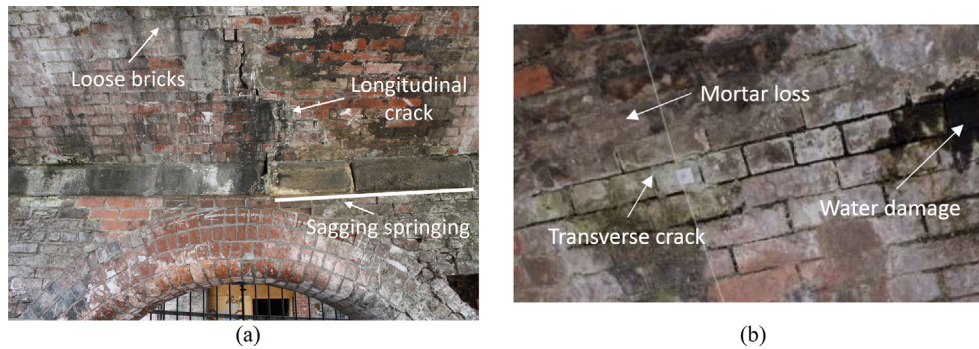


Fig. 6. Bridge defects: (a) central dipping of relieving arch between Arches 37 and 38, seen from Arch 38 and (b) transverse crack at the western quarter span of Arch 38.

Table 5

Measured current geometry of Marsh Lane Viaduct.

		Arch 39		Arch 38		Arch 37	
Arch radius of curvature (m)		5.877		6.019		5.731	
Arch axis inclination, $\theta_y$ (°)		−0.01		0.53		0.22	
Spandrel wall inclination, $\theta_y$ (°)	North	1.62		1.82		1.40	
	South	0.03		−0.91		−1.09	
		Western pier east face		Eastern pier west face		Western pier east face	
Pier inclination, $\theta_x$ (°)		0.260		0.501		0.124	
Magnitude of potential horizontal springing displacement relative to the ground (mm)		24		45		11	

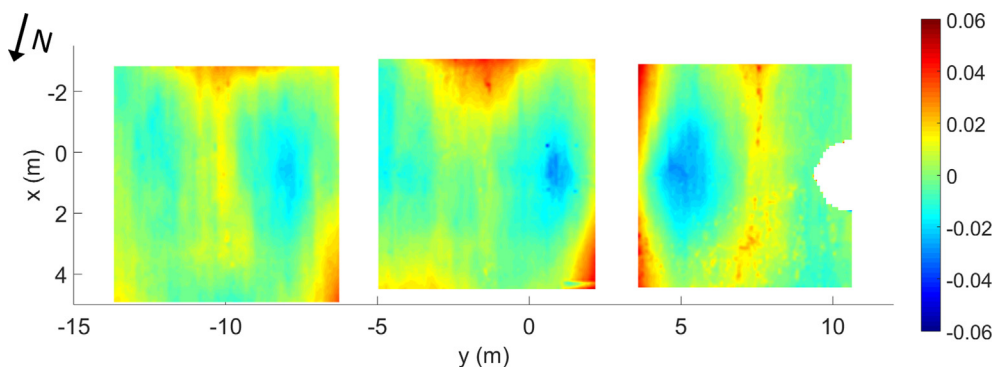


Fig. 7. Plan view 3D error map (Left to right: Arch 39 to 37; colour bar values in m).

and circles were fitted to the arch barrels. The resulting fitting parameters are shown in Table 5. According to these results, the radius of curvature for all three arches was around 6 m. Arches 37 and 39

demonstrated negligible inclination of the transverse arch axis (see  $\theta_y$  in Fig. 2b) while Arch 38 demonstrates close to 0.5 degrees of inclination.

Spandrel wall plane fits revealed observable tilting of spandrel

walls, though not enough to cause safety concerns. Positive  $\theta_y$  inclination indicates rotation towards the north, and vice versa. In general, the north spandrel walls were inclined northwards and the south spandrel was inclined southwards for the three arches.  $\theta_x$  inclination of the piers from plane fit implied potential horizontal movements of springing points, which were calculated by multiplying pier height of 5.2 m and the angle  $\theta_x$ . Interestingly, the results demonstrated that all of the piers were inclined in the same (positive) direction. However, different results were obtained for western and eastern faces of the same pier between Arches 37 and 38. Following inspection of partial plane fits to sections of the point cloud, it became clear that significant repointing on the piers influenced the pier inclination results. Therefore, the pier inclination data is not examined further.

#### 4.1.4. Step 4 – Error mapping

Fig. 7 shows the 3D error map fit of the three arches, rotated to be approximately parallel to each other on the XY plane. The missing section in Arch 37 was due to a relieving vault component, which was manually cropped from the arch barrel point cloud data during segmentation. Fig. 7 shows clear distortion of the arch barrels. In Arch 38 and Arch 37, the blue areas above the relieving arches suggest local downward depressions (maximum of 5 cm fitting error) with respect to the fitted shape. The blue areas correspond to the loose bricks observed at the same locations of the bridge in the field work (see Fig. 6a). It is interesting that the longitudinal crack, which is up to 5 cm wide, is not visible from these scans. This is likely due to the smoothing function used to create the error map and the lack of points inside the crack. Cracks of such large magnitude could be captured by laser scanner, if desired, by increasing the point cloud resolution and changing the parameter of the Gridfit smoothing function employed, but this was not necessary for this study.

Additionally, there appears to be a systematic concentration of fitting errors in the area between Arches 38 and 37, where the fitting errors increase up to 6 cm on both sides of the pier. These red triangular areas indicate the likely presence of 3D differential settlements, caused by increased sagging above the relieving arch. Further analyses in this section focus on investigating 2D slices from Arches 38 and 37 to clarify these observations. Arch 39 features lesser distortion (see Fig. 7), which is in accordance with lesser cracking observed in this arch. It also has a different boundary condition in that its eastern support is similar to an abutment, providing significantly stiffer support. Therefore, further investigation of Arch 39 was not pursued in this study.

Fig. 8 examines 2D point cloud strips situated along the transverse axis of the Arches 38 and 37 of the bridge, for the springing, quarter span and crown areas. As observed earlier, a significant elevation dip is evident from the data around the pier between Arches 38 and 37. This is observed in the western springing transverse strip of Arch 38 and the eastern springing of Arch 37. It is important to note that these transverse strips are not demonstrating a linear elevation profile and are indicative of support settlements. In contrast, the crown strip of Arch 38 shows a more linear profile, which relates to the overall inclination of the arch axis identified earlier with fitting parameters in Table 4.

Fig. 9 shows the longitudinal point cloud strips from Arches 38 and 37 (blue lines) fitted with a circle (red lines). The strips are across the arch width and located under the spandrel walls, tracks and bridge longitudinal centreline. In addition, the 2D error (green points) is plotted on the point cloud and fitted circle with a magnification factor of 100. It is interesting to note that all longitudinal strips from Arches 38 and 37 demonstrate a characteristic distortion signature. This distortion signature is stronger in the northern and central portions of both arches, and is less clear in the southern section. Comparing shapes from corresponding strips of different arches reveals that the distortion shapes are mirror images of one another about the vertical axis passing through the crown.

#### 4.1.5. Step 5 – Structural evaluation

While the fitting parameters (4.1.3) and error maps (4.1.4) revealed consistent anomalies and distortion patterns that correlate with field observations, historic support movements have not been identified yet. To achieve this, the procedure discussed in 3.5.4 is followed. In its first phase, this involves identifying hinges from the 2D error maps and verifying them with field observations.

In all of the error maps presented in Fig. 9, two kinks are evident: one near the quarter span (approx. 1.8 m and 1.9 m from the west springing for Arch 38 and east springing for Arch 37, respectively) and the other one close to the crown (approx. 3.9 m and 4.1 m from the west springing for Arch 38 and east springing for Arch 37, respectively). These kinks indicate extrados hinges at the western quarter span for Arch 38 and at the eastern quarter span for Arch 37. The kink at the crown is less well-defined and may be closer to the opposing quarter span, potentially indicating a more distributed change in curvature of the real arch between the crown and the quarter span, rather than a distinct hinge. With intrados hinges at the crown and springing points on the pier between 38 and 37, a partial asymmetric mechanism could form to accommodate the support movements. The hypothesised presence of an extrados hinge at the quarter span is supported by visual observations (see Fig. 6b) as well as dynamic strain and displacement measurements from these arches where crack closing is observed during train passage [28].

On the basis of these hinge locations, support movements are identified with the help of Tables 3 and 4. It is unlikely for the investigated spans to experience horizontal span opening and closing due to large stiffness of Arches 38 and 37 against this type of movement. This statement is supported by the lack of discernible patterns for pier orientation in Table 4. Therefore, it is hypothesised that the movement is dominated by vertical settlement of the pier between Arches 38 and 37. This is supported by the symmetry between the error maps observed for both arches; symmetric mechanisms are unlikely to have occurred if lateral movements were significant, since span opening and closing mechanisms differ significantly for arches supported with a backing [7]. Fig. 10 demonstrates the identified error maps that result from 2D fitting of theoretical kinematic mechanisms for longitudinal slices under the bridge centreline and under the tracks. The structures are assumed to have a span of 7.7 m and a radius of curvature of 6.0 m. As a result of the analyses, a 4 cm settlement of the pier at the bridge longitudinal centreline is hypothesised for both arches under the bridge centreline (Fig. 10a and b). Small kinks can be observed in the real data, likely relating to construction tolerances as well as brickwork ageing and deterioration, which are not captured by the theoretical mechanisms. However, a good overall agreement is observed between the error maps obtained from real point clouds and theoretical mechanisms for both arches, validating the approach. A similar conclusion can be reached for the evaluation of error maps for slices under the southern tracks. Here, the theoretical mechanisms indicate a reduced vertical settlement of 2.5 cm at the pier between 38 and 37, compared to the vertical settlement at bridge centreline. It is interesting to note that the identified vertical settlements demonstrate similar trends to the elevation drops in the transverse slices, observed earlier in Fig. 8, providing confidence in the results.

Fig. 11 summarises the identified support movements. A longitudinal section cut of the point cloud from the bridge longitudinal centreline in Fig. 11a shows the vertical settlement and the mechanism it induces in the arch barrel. The settlement was due to the progressive sagging of the relieving arch during service loading, which caused the formation of the longitudinal crack. In addition, Fig. 11b demonstrates a plan view, illustrating the identified differential support movements for all the investigated longitudinal slices. In addition to the concentration of vertical settlements around the relieving arch, this figure indicates an overall settlement of the pier of 2 cm. These inferred vertical displacements demonstrate similar trends with the elevation of transverse slices (relative to the southern corner) in Fig. 11c, indicating

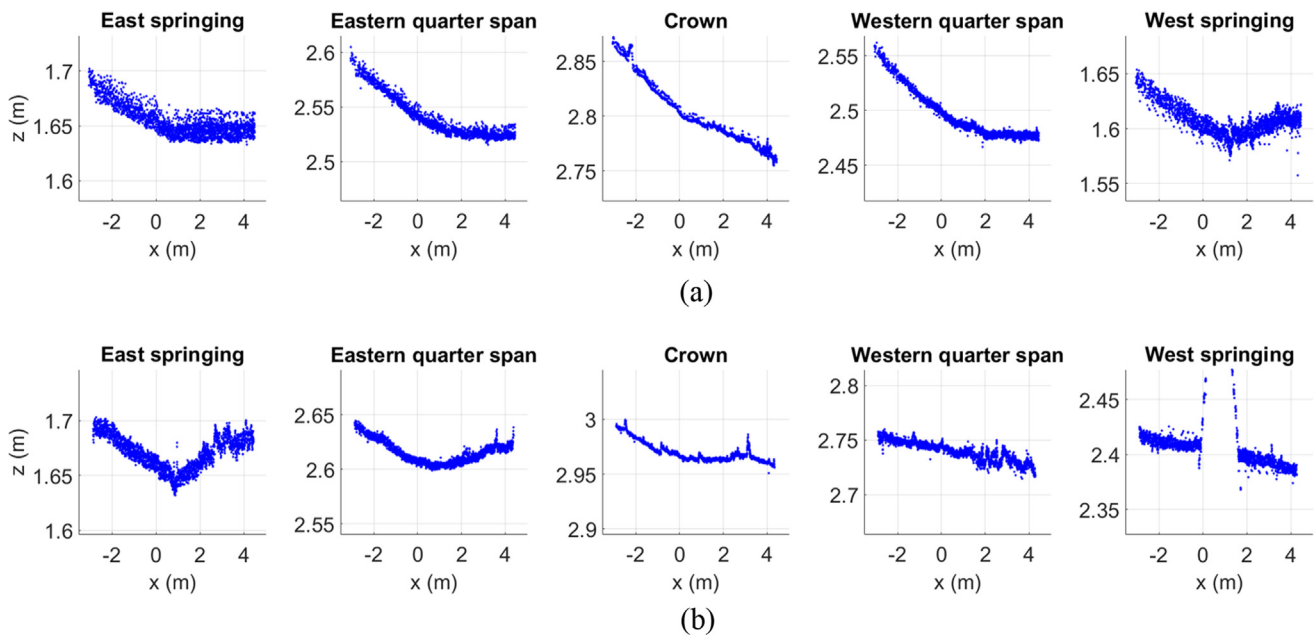


Fig. 8. Transverse profiling of transverse arch strips: (a) Arch 38 and (b) Arch 37.

that the relative differences in elevation along the transverse length is partially attributable to settlements.

#### 4.2. Case study 2 – Stapleton Road Viaduct, Bristol

##### 4.2.1. Step 1 – Preliminary bridge information

The Stapleton Road Viaduct is a four span masonry arch rail bridge in Bristol, UK (see Fig. 12). It was initially constructed in 1863 to carry a single line, and was widened in 1874 towards the east to carry an additional line. Two of the four arches at the north end of the viaduct were investigated in this project. These arches are segmental in form, have negligible skew and span approximately 8 m. The northern arch is supported by an abutment with a wing wall and a pier, while the southern arch is supported by piers on both sides. Two notable cracks are observed on the bridge intrados: an obvious longitudinal crack

divides the old and new parts of the arch (see Fig. 12a), while a diagonal crack extending between the crown and quarter span is present in the new part of the northern span. In addition, Fig. 12a demonstrates remedial works with steel ties, which have been used to tie the old and new parts and prevent relative movement of the spandrel walls.

##### 4.2.2. Step 2 – Laser scan data acquisition and point cloud processing

Laser scan data was collected in August 2012 and processed in accordance with Section 3.2. The processed point cloud for these arches are shown in Fig. 13b.

##### 4.2.3. Step 3 – Primitive shape fitting

Similar to the previous case study, planes were fitted to the piers and spandrel walls, while cylinders and circles were fitted to the arch barrels. A single cylinder fit was conducted for each span of the arch

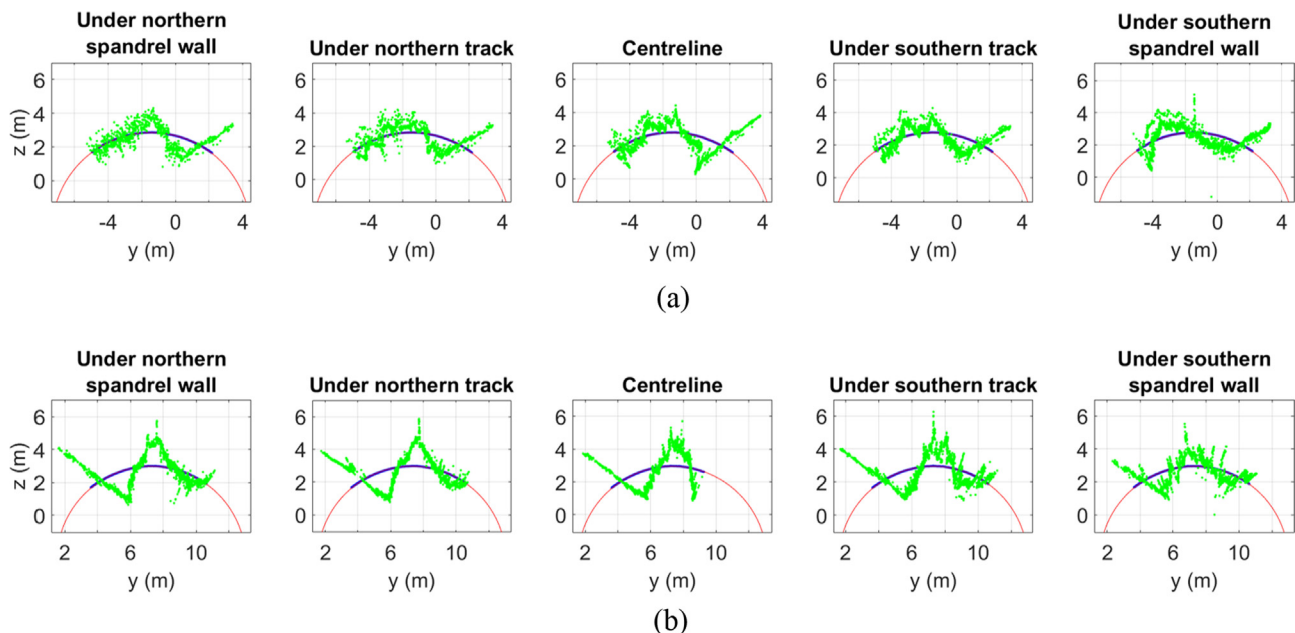
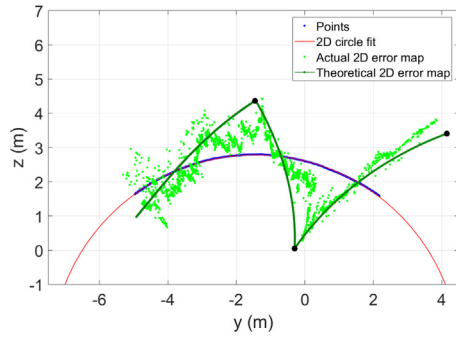
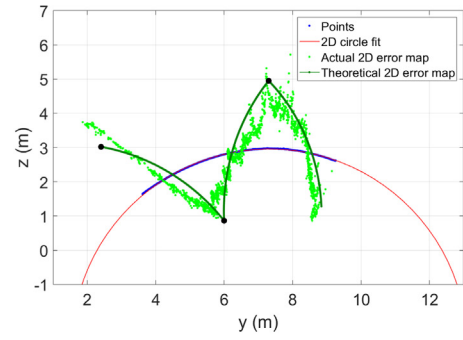


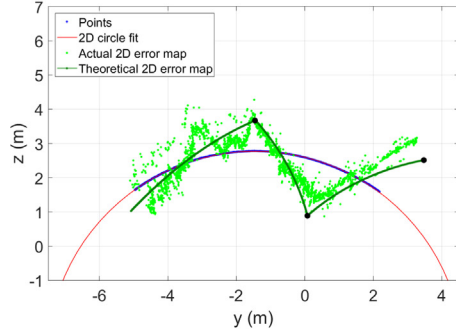
Fig. 9. 2D curve fit and deformed geometry of longitudinal arch strips: (a) Arch 38 and (b) Arch 37.



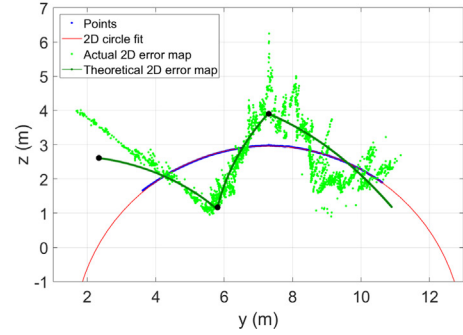
(a) Arch 38, centreline, relative west (right) pier settlement of 4 cm



(b) Arch 37, centreline, relative east (left) pier settlement of 4 cm

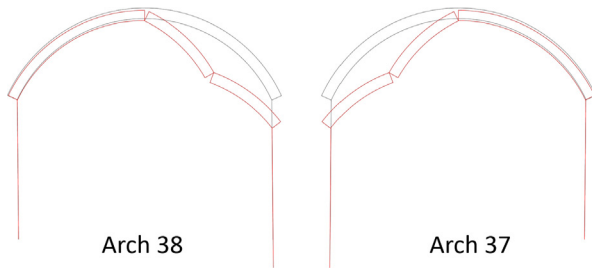


(c) Arch 38, under southern track, relative west (right) pier settlement of 2.5 cm

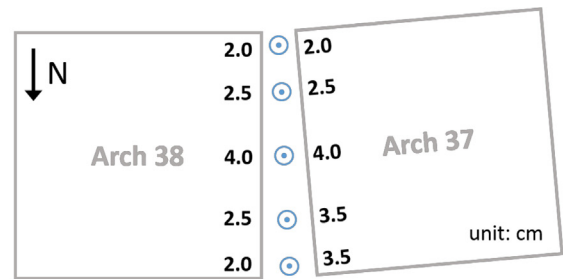


(d) Arch 37, under southern track, relative east (left) pier settlement of 2.5 cm

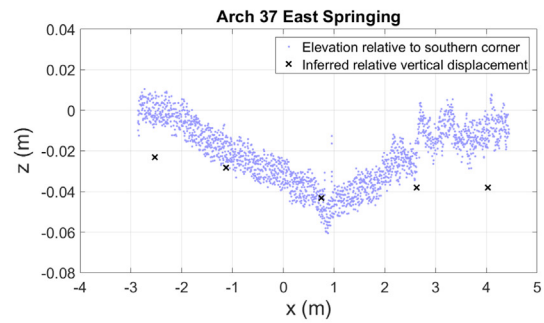
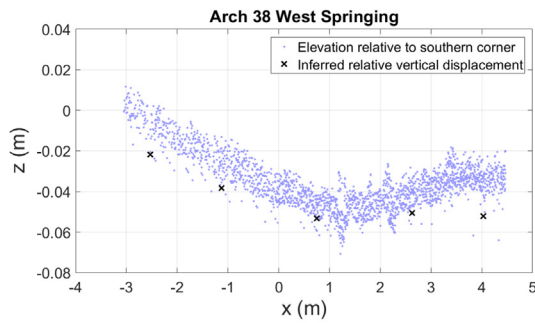
Fig. 10. Comparison of actual and theoretical deformed geometry: (a)–(d).



(a)



(b)



(c)

Fig. 11. (a) a schematic showing the identified arch mechanism and support movements for the bridge longitudinal centreline section, (b) a plan view demonstrating the vertical support movements along the bridge transverse length determined using the method demonstrated in Fig. 10 and (c) a comparison of the elevation of transverse slices at the springing points and the inferred vertical support movements.



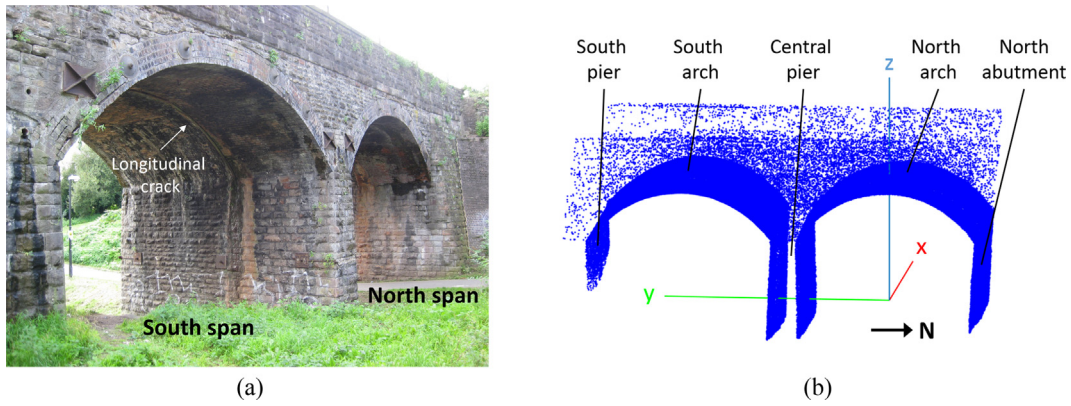


Fig. 12. Stapleton Road Viaduct: (a) view from the East and (b) labelled point cloud.

initially (see Table 6). The error maps obtained from this approach (see Section 4.2.4) highlighted the distinct behaviour of the old and new sections of each span. Thereafter, fittings were done separately for the old and new parts of the bridge, which indicated that both parts have similar radii of curvature of 4.8 m, but have a consistent inclination difference of  $-0.6$  degrees. This inclination is likely the cause of the separation between two sections of the bridge, which caused the longitudinal crack (see Fig. 12a). It may have occurred during construction of the enlargement or shortly after due to soil consolidation or

live loading. The water stains on the bridge concentrating around this crack indicate the presence of active degradation in this area. The schematic in Fig. 13a summarises these rotations from the primitive shape fits (shown as  $\Delta\theta_i$ ).

Plane fits were conducted for the western and eastern faces of the piers and spandrel walls. Plane fit results presented in Table 6 indicate that both spandrel walls rotate towards the bridge longitudinal centreline. Here, a positive  $\theta_y$  rotation indicates a movement towards the west and vice versa. Plane fits of the intermediate pier ends (last row of

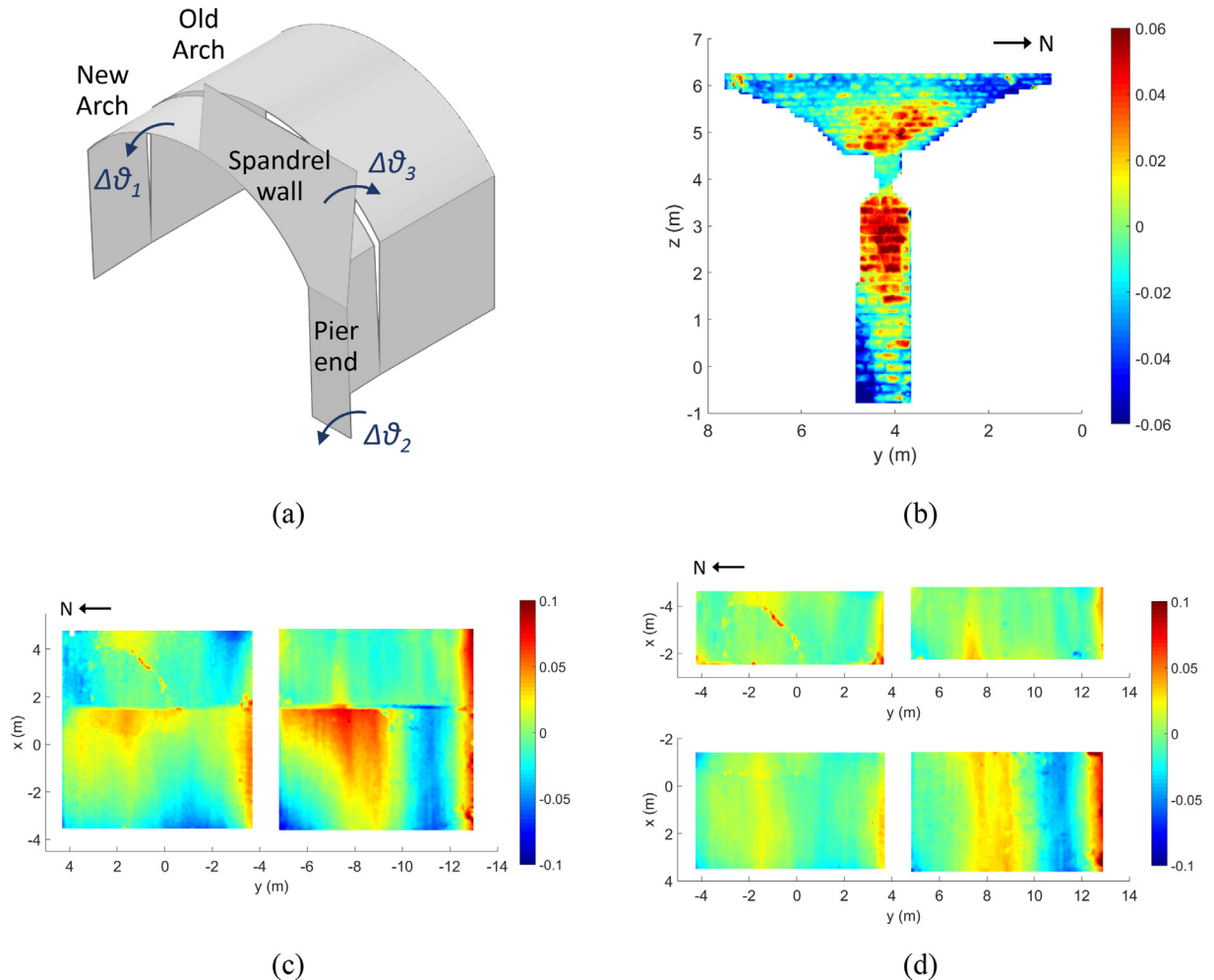


Fig. 13. (a) Diagram of hypothesised rotations of the new arch, the east pier end and the east spandrel wall relative to the reference geometry, (b) 3D plane fit error map of east face of intermediate pier and associated spandrel wall, (c) 3D arch fit error map of whole arches and (d) 3D arch fit error map of new and old arches (colour bar value in m).

**Table 6**  
Measured current geometry of the bridge.

	North span		South span	
	Full north arch		Full south arch	
Arch radius of curvature (m)	4.795		4.839	
Arch axis inclination, $\theta_y$ (°)	0.47		1.02	
	Old north arch (West)		Old south arch (West)	
Arch radius of curvature (m)	4.733		4.916	
Arch axis inclination, $\theta_y$ (°)	0.46		1.09	
	New north arch (East)		New south arch (East)	
Arch radius of curvature (m)	4.841		4.787	
Arch axis inclination, $\theta_y$ (°)	-0.17		0.49	
Arch rotation relative to the old arch, $\Delta\theta_y$ (°)	-0.63		-0.60	
	Old Arch, North abutment – south face	Old Arch, Central pier – north face	Old Arch, Central pier – south face	Old Arch, South pier – north face
Pier inclination of, $\theta_x$ (°)	3.75	-0.84	1.72	-1.13
Deduced pier rotation, $\theta_x$ (°)	0	0.45		0.10
Magnitude of potential horizontal springing displacement relative to the ground (mm)	0	39		5
Spandrel wall inclination, $\theta_y$ (°)	East	1.36		1.74
	West	0.05		-0.46
Intermediate pier side/end face inclination, $\theta_y$ (°)	East	n/a	-0.0009	n/a
	West	n/a	-2.1332	n/a

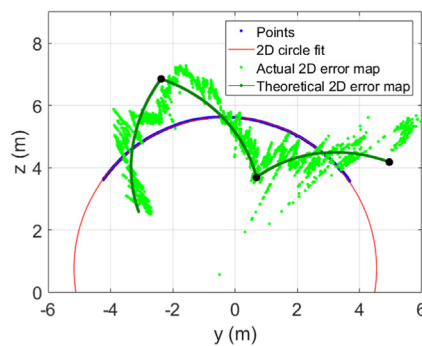
Table 6) indicate that the East pier end is nearly vertical, while the West pier end is rotating towards the bridge centreline. However, if the pier ends were originally inclined, this could potentially indicate an overall rotation towards the East. The hypothesised rotations of the East pier end and spandrel wall are also summarised in Fig. 13a (shown as  $\Delta\theta_2$  for the pier end and  $\Delta\theta_3$  for the spandrel wall). Plane fits were also done for the southern and northern faces of the piers. However, these are influenced by the tapered design of the piers, which are visible in the laser scan point cloud of Fig. 12b. The mean plane of the tapered point clouds on either side of the pier were used to obtain an indication of plane tilt of the old arch piers in Table 6. However, the tapered design was also present in the abutment, and therefore it was not possible to utilise this tilt to infer potential springing displacements at the abutment. The abutment lateral displacements were assumed as zero (see Table 4), and the magnitude of potential horizontal springing displacement relative to the ground was calculated for the piers. This indicated that the pier in between the north and south spans may have moved laterally, but there is very little suggestion that the southern pier of the south arch has experienced movements.

#### 4.2.4. Step 4 – Error mapping

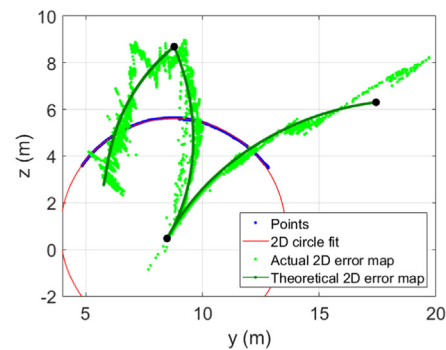
An error map of the plane fit of the eastern face of the pier and eastern spandrel wall is presented in Fig. 13b. In this figure, positive errors indicate movement of the region in the positive x-direction, away from the bridge centreline. The plane fits demonstrate that the pier end (lower half of image) is nearly vertical (see Table 6), while the spandrel wall is rotating significantly towards the west. Thus, when a single plane is fitted to the spandrel wall and the pier end combined, the top of the pier end (red-coloured area in Fig. 13b) appears to bulge towards

the viewer, while the top of the spandrel wall rotates away. This outward “kink” at the top of the pier is clearly visible on site. If the pier ends were initially inclined, this confirms that the “new” arches and piers are rotating away from the old portion. However, due to differential rotations between the arch and the pier, spandrel wall rotates inwards towards the bridge centreline.

The 3D circular cylinder fits in Fig. 13c to the whole bridge indicated that each arch consists of two parts. Thus, a second round of 3D circular cylinder fit was carried out for each part, as shown in Fig. 13d. The old part of the bridge displays more noticeable errors and the south arch appears more distorted than the north arch. Further examinations will therefore focus on the old part of the arches. In addition, two differences can be highlighted between the patterns observed in the previous case study (Section 4.1) and the current one. Firstly, the 3D error maps display a banded profile which show negligible variation along the width. This shows that a single 2D longitudinal slice is sufficient to examine the distorted bridge geometry for the old part of the arch. Secondly, a “crack” is visible in the new part of the arch in Fig. 13d, which indicates the highest error values. This crack is visible in the point clouds because entire bricks had fallen from the arch intrados at this location, so several laser points were retrieved from the inside the crack and the width of the crack was enough to not be eliminated by smoothing functions. In addition, longitudinal slices were obtained from the longitudinal bridge centreline of the old part of the arch for the two spans. 2D circle fits were then conducted, and the results are presented in Fig. 14. The distortion profiles indicated by the two arches are somewhat similar, although they differ in magnitude.



(a) North Arch: north (left) end rigid; pure south end settlement of 6 cm; hinge locations: 1/3 span, 2/3 span, south end



(b) South Arch: north (left) end rigid; pure south end settlement of 8 cm; hinge locations: 1/2 span, 3/4 span, south end

Fig. 14. 2D deformed geometry for mid-longitudinal strips of old portion of each arch and potential arch mechanisms: (a) and (b).

#### 4.2.5. Step 5 – Structural evaluation

It is now necessary to evaluate the distortion patterns to identify potential support movements using the procedure discussed in Section 3.5.4. In Fig. 14, it can be seen that the 2D error maps feature kinks. For the north arch, these are located at thirds of the span. For the south arch, one of the hinges is clearly located at the northern quarter span and the other one is located in between the crown and the southern quarter span. For simplicity, the second hinge is assumed at the crown. For both arches, the third hinge is located at one of the springings. The third hinge is assumed at the southern springing point for the north arch. For the southern arch, the third hinge is also assumed to be located at its southern springing point, since significant distortions are concentrated on this corner. Due to repointing and widespread water ingress issues in the arch, no clear indication of an extrados hinge visible on the arch intrados (as indicated by the circle fits) was observed. To validate the presence of such a hinge, additional strain and displacement measurements during loading may be beneficial, as in the previous case study in Section 4.1.

With these hinge locations, it is now possible to hypothesise potential support movements. The real support movements are likely to involve both horizontal and vertical components. However, in the absence of further information, pure horizontal and vertical settlement scenarios are considered, in accordance with Table 4. When horizontal support movements are considered, both spans appear to be opening. The inferred relative horizontal displacements are 3 cm and 5 cm respectively for the north and south arches. This implies 8 cm of total movement of the southern pier. The other investigated possibility involves the vertical settlement of the intermediate and southernmost piers. The inferred vertical movements for these piers are 6 cm and 14 cm respectively relative to the abutment. This indicates a relative settlement of 8 cm for the southern arch. In reality, a combination of horizontal and vertical support movements may have been experienced which would result in smaller vertical displacements to achieve the distorted shape. Similar to the rotations of the arch axis, the identified vertical support movements may be related to the later construction of the new section of the bridge to increase its width, as well as the foundation conditions of the investigated arches.

## 5. Conclusions

This paper proposes a new assessment method, which aims to infer potential historic support movements of masonry arch bridges from laser scan point clouds of their current geometry. The proposed technique involves processing and primitive shape fitting of point clouds to identify anomalies in bridge geometry. These anomalies are then related to historic support movements with the knowledge of typical construction practices and simple kinematic analyses. The assessment

method is described with a simple workflow and yields quantitative support movement estimations. In the final step of the method, key settlement indicators (bedding joint inclinations, crack locations, mirroring patterns in neighbouring arches and theoretical estimations of hinge locations) are examined in order to evaluate potential support movement scenarios.

The application of the assessment method to two case studies clarified behaviour of the bridges, and quantified the support movements which could potentially explain the existing damage in the bridge. In the first case study, a relieving arch in the piers sagged due to progressive loading, causing differential settlements along the pier width. Using the assessment method, the hinges which formed in the arch barrel were identified, and were validated with field measurements. The kinematic analyses were then used to identify the magnitude of vertical support movements due to the sagging of the relieving arch, along the width of the bridge. Elevation differences along the transverse bedding joints, and matching mechanisms in neighbouring arches, validated the identified mechanism. In a second case study, the influence of the enlargement of a bridge viaduct was highlighted. The fitted primitive shapes helped identify the relative rotation between the new and old parts of a bridge. In addition, analysis of the support settlements identified various support movements which could explain observed distortions. In particular, the locations of identified hinges were related to predictions of hinge locations for different support movements, to suggest the predominant role of vertical support settlements in causing the distortions. In both case studies, identification of the support movements and the induced mechanisms were useful to understand existing damage and may inform future assessments of serviceability response.

## Acknowledgements

The work carried out was funded by EPSRC and Innovate UK, through the Cambridge Centre for Smart Infrastructure and Construction (Grant Reference Number EP/L010917/1). The authors would like to acknowledge Mark Norman of Network Rail for his support. They would additionally like to thank Jason Shadelow, Kenichi Soga and Giuseppe Narciso for their assistance in data collection.

## Appendix A. Supplementary material

Supplementary data associated with this article can be found, in the online version, at <https://doi.org/10.1016/j.engstruct.2018.06.094>.

## References

- [1] Urban Z. Assessment, reliability and maintenance of masonry. In: Roca P, Molins C,

- editors. Arch Bridges IV-Advances in Assessment, Structural Design and Construction, Barcelona. 2004.
- [2] Sarhosis V, De Santis S, de Felice G. A review of experimental investigations and assessment methods for masonry arch bridges. *Struct Infrastruct Eng* 2016;12(11):1439–64.
  - [3] McKibbins LD, Melbourne C, Sawar N, Gaillard CS. CIRIA C656. Masonry arch bridges: condition appraisal and remedial treatment; 2006.
  - [4] LimitState Ltd. LimitState: RING manual Version 3.1b; 2014.
  - [5] Heyman J. The stone skeleton. *Int J Solids Struct* 1966;2(2):249–79.
  - [6] Brencich A, Morbiducci R. Masonry arches: historical rules and modern mechanics. *Int J Architect Heritage* 2007;1(2):165–89.
  - [7] Acikgoz S, Soga K, Woodhams J. Evaluation of the response of a vaulted masonry structure to differential settlements using point cloud data and limit analyses. *Constr Build Mater* 2017;150:916–31.
  - [8] Quintero M, Van Genechten B, De Bruyne M, Poelman R, Hankar M, Barnes S, et al. Theory and practice on terrestrial laser scanning; 2008.
  - [9] Schueremans L, Van Genechten B. The use of 3D-laser scanning in assessing the safety of masonry vaults – a case study on the church of Saint-Jacobs. *Opt Lasers Eng* 2009;47(3–4):329–35.
  - [10] Riveiro B, DeJong MJ, Conde B. Automated processing of large point clouds for structural health monitoring of masonry arch bridges. *Autom Constr* 2016;72:258–68.
  - [11] Lubowiecka I, Armesto J, Arias P, Lorenzo H. Historic bridge modelling using laser scanning, ground penetrating radar and finite element methods in the context of structural dynamics. *Eng Struct* 2009;31(11):2667–76.
  - [12] Riveiro B, Morer P, Arias P, De Arteaga I. Terrestrial laser scanning and limit analysis of masonry arch bridges. *Constr Build Mater* 2011;25(4):1726–35.
  - [13] Girardeau-Montaut D, Roux M. Change detection on points cloud data acquired with a ground laser scanner. Enschede: International Archives of Photogrammetry, Remote Sensing and Spatial Information Sciences; 2005.
  - [14] Lague D, Brodu N, Leroux J. Accurate 3D comparison of complex topography with terrestrial laser scanner: application to the Rangitikei canyon (N-Z). *ISPRS J Photogramm Remote Sens* 2013;82:10–26.
  - [15] Teza G, Galgaro A, Zaltron N, Genevois R. Terrestrial laser scanner to detect landslide displacement fields: a new approach. *Int J Remote Sens* 2007;28(16):3425–46.
  - [16] Acikgoz MS, Pelecanos L, Giardina G, Aitken J, Soga K. Distributed sensing of a masonry vault during nearby piling. *Struct Control Health Monitor* 2016;24(3):1–19.
  - [17] Gordon SJ, Lichti DD. Modeling terrestrial laser scanner data for precise structural deformation measurement. *J Surv Eng* 2007;133(2):72–80.
  - [18] Cabaleiro M, Riveiro B, Arias P, Caamaño JC. Algorithm for beam deformation modeling from LiDAR data. *Measure J Int Measure Confed* 2015;76:20–31.
  - [19] Pesci A, Casula G, Boschi E. Laser scanning the Garisenda and Asinelli towers in Bologna (Italy): detailed deformation patterns of two ancient leaning buildings. *J Cult Heritage* 2011;12(2):117–27.
  - [20] Pesci A, Teza G, Bonali E, Casula G, Boschi E. A laser scanning-based method for fast estimation of seismic-induced building deformations. *ISPRS J Photogramm Remote Sens* 2013;79:185–98.
  - [21] Teza G, Pesci A. Geometric characterization of a cylinder-shaped structure from laser scanner data: development of an analysis tool and its use on a leaning bell tower. *J Cult Heritage* 2013;14(5):411–23.
  - [22] Pendrigh S. Analysis of masonry structures via the use of point clouds. University of Cambridge; 2013.
  - [23] Armesto J, Roca-Pardiñas J, Lorenzo H, Arias P. Modelling masonry arches shape using terrestrial laser scanning data and nonparametric methods. *Eng Struct* 2010;32(2):607–15.
  - [24] Conde B, Drosopoulos GA, Stavroulakis GE, Riveiro B, Stavroulaki ME. Inverse analysis of masonry arch bridges for damaged condition investigation: application on Kakodiki bridge. *Eng Struct* 2016;127:388–401.
  - [25] Riley E. The Telford bridge at over. University of Cambridge; 2015.
  - [26] Arun KS, Huang TS, Blostein SD. Least-squares fitting of two 3-D point sets. *IEEE Trans Pattern Anal Mach Intell* 1987;9(5):698–700.
  - [27] Kasa I. A Circle Fitting Procedure and Its Error Analysis. *IEEE Trans Instrum Meas* 1976;25(1):8–14.
  - [28] Acikgoz S, DeJong MJ, Kechavarzi C, Soga K. Dynamic response of a damaged masonry rail viaduct: measurement and interpretation. *Eng Struct* 2018;168:544–58.
  - [29] Acikgoz S, DeJong MJ, Soga K. Sensing dynamic displacements in masonry rail bridges using 2D digital image correlation. *Struct Control Health Monitor* 2018. <https://doi.org/10.1002/stc.2187>.